Inorganic Chemistry Communications 183 (2026) 115877

Contents lists available at ScienceDirect

Inorganic Chemistry Communications

journal homepage: www.elsevier.com/locate/inoche

Research Article

Enhanced fluoride adsorption using NiO/Solanum tuberosum peels nanocomposites, insight into Box-behnken design (BBD) analysis and application in water defluoridation

Mukhtar Ahmad [a,*], Khurram Shehzad [b], Ghulam Abbas Ashraf [c], Muhammad Iqbal Asif [a], Doniyor Jumanazarov [d], Farruh Atamurotov [e,f], Ahlem Guesmi [g], Imed Boukhris [h], Rizwan ul Hassan [i,*]

[a] Department of Physics, COMSATS University Islamabad, Lahore Campus, Lahore 54000, Pakistan
[b] Institute of Solid-State Physics and Key Laboratory of Photovoltaic and Energy Conservation Materials, Hefei Institutes of Physical Science, Chinese Academy of Sciences, Hefei, Anhui 230031, PR China
[c] Low Dimensional Materials Research Center at Khazar University, AZ1096 Baku, Azerbaijan.
[d] Urgench State University, Kh. Alimdjan Str. 14, Urgench 220100, Uzbekistan
[e] Kimyo International University in Tashkent, Shota Rustaveli str. 156, Tashkent 100121, Uzbekistan
[f] University of Tashkent for Applied Sciences, Str. Gavhar 1, Tashkent 100149, Uzbekistan
[g] Chemistry Department, College of Science, Imam Mohammad Ibn Saud Islamic University (IMSIU), P.O. Box 5701, Riyadh 11432, Saudi Arabia
[h] Department of Physics, Faculty of Science, King Khalid University, P.O. Box 9004, Abha, Saudi Arabia
[i] Department of Chemical and Biological Engineering, Gachon University, Gyeonggi-Do 13120, Republic of Korea

ARTICLE INFO

Keywords:
NiO/potato peels nano composites
Hydrothermal process
X-ray diffraction
Kinetics models
Chemical adsorption
Statistical analysis

ABSTRACT

A novel NiO/potato peels nanocomposite was successfully synthesized via a facile hydrothermal process for the efficient removal of fluoride from water. The structural and morphological properties of the composite were confirmed by XRD, FTIR, and SEM. Adsorption kinetics followed a pseudo-second-order model, indicating chemisorption as the dominant mechanism. Response Surface Methodology (RSM) based on a Box-Behnken Design (BBD) was employed to optimize the adsorption process. The optimal conditions for maximum fluoride adsorption were determined to be an adsorbent dosage of 1 g/L, a pH of 7, and a contact time of 480 minutes. Under these optimized conditions, the nanocomposite achieved a high adsorption capacity and reduced fluoride concentration below the WHO permissible limit of 1.5 mg/L within just two hours. The composite also exhibited excellent regeneration capability over five cycles. This study demonstrates the potential of this sustainable, waste-derived nanocomposite as a highly effective adsorbent for fluoride remediation in water.

1. Introduction

The air and water, which are essential for the survival of living things, are contaminated by the numerous industrializations of the modern era. The need for safe drinking water is becoming more critical as the water level decreasing rapidly [1]. Natural causes and human activity are the two main causes that fluoride poisoning of water resources. Ground and surface waters can become contaminated by fluoride, which is commonly found in rocks and can be eroded away by rainfall. However, fluoride contamination can be found in a variety of industrial wastewaters from the production of steel and aluminum, metal finishing and electroplating, glass and semiconductors, mineral beneficiation, and fertilizer operations [2]. Both humans and animals require fluoride (F^{-1}), but the amount of fluoride in drinking water must not exceed specific thresholds [3]. The World Health Organization (WHO) suggests that 1.5 mg/L of fluoride is the highest permissible content [4]. Excessive fluoride consumption can have negative consequences on neuro transmitters, dental and skeletal fluorosis. Numerous procedures including adsorption [5,6], membrane approaches [7], ion exchange [8], electrocoagulation [9], and precipitation [10] have been used for fluoride removal. Adsorption is one of the technologies that has been shown to be an efficient, cost-effective, and ecologically benign way to remove excessive fluoride from drinking water due to its simplicity, effectiveness, and affordability [11].

* Corresponding authors.
E-mail addresses: ahmadmr25@yahoo.com, mukhtarahmad@cuilahore.edu.pk (M. Ahmad), rizwanhassan72@gmail.com (R. Hassan).

https://doi.org/10.1016/j.inoche.2025.115877
Received 7 October 2025; Received in revised form 17 November 2025; Accepted 19 November 2025
Available online 23 November 2025

It was discovered recently that the biomass derived from walnut and blue pine might eliminate heavy metal ions from surface waters [12]. There have also been reports of water pollutants being removed from water by scales of fish, fibers of coconut, dried water hyacinth plant roots, Moringa oleifera and, bird feathers, Momordi cacharantia seeds powder, powdered eggshells [13], hair of human [14], husk of rice [15], and polish of rice [16]. Potato, likewise known as Azedarach India, is a big, evergreen plant that is regarded as a "Saratoga Navarino" (remedy for all diseases). Similarly reports of potato peel's ability to adsorb copper have been reported in publications [17,18]. Globally, potatoes rank fourth in the context of fresh food production and are the most extensively planted tuber crop. But its peel may not be as useful. Ash made from potato peels may have a large surface area, making it a good material for fluoride adsorption. Potato peels are used as bio-sorbents for the adsorption of fluoride since they are naturally abundant and affordable. In this study, we used NiO/potato peel composite, as an active adsorbent to remove fluoride from water. Potato Peel has a porous structure and so can absorb more fluoride ions from water [19].

Nanotechnology can be used to clean wastewater by removing various impurities in it [20]. Nanoparticles are special for their off-the-shelf use because the nano process removes all impurities [21]. The high specific surface area, rapid disintegration, strong reactivity, and strong adsorption of nanoparticles make water visible and make it cost-effective to use nanotechnology for wastewater treatment [22–24]. An important part of the rapid development of nanotechnology is the production of nanoparticles and nanoproducts with specific and size-dependent physicochemical properties, unlike bulk products [25]. Many successful applications in biomedicine, cosmetics, healthcare, renewable energy, and environmental remediation take advantage of the unique properties of nanoparticles [26]. Nanoparticles have excellent optical, electrical, magnetic, and catalytic abilities due to their high volume-to-volume ratios compared to bulk materials [27]. One of the primary objectives in chemistry has been the production of nanoparticles (NPs) with precise control over their diameter, structure, and crystallinity [28–30]. Only a few possible applications for these NPs include biosensors, bio-medical devices, low-cost electrodes, and catalysts for bacterial biotoxin clearance [31]. Nano-metal oxides with diameter range 1 to 100 nm are a family of metal oxide material. Nano-metal oxide is typically more affordable, environmentally safe, and have better redox and adsorption capabilities. Recently, nano-metal oxides was synthesized and used to deal with environmental problems [32]. In addition to an enhancement in surface functional groups, comparison to the unmodified material, The treatment of biochar with nano-metal oxides results in increased specific surface area, enhanced cation exchange capacity, and improved porosity. Modified biochar's ability to absorb contaminants changes based upon the kind of nano-metal oxide involved [33]. NiO with potato peels combining the advantages of nano-metal oxides and biochar, and perform better than unmodified oxide in terms of mobility, crystallite size, and electron transfer capacity [34]. Since they have both chemical and magnetic characteristics, nickel oxide nanoparticles (NiO NPs) are important metallic oxide [35–37].

Technology has recently recognized the value of NiO synthesis. Consequently, there are many methods for producing Nickel oxide particles, such as ball milling [38], sol–gel [39], co-precipitation [40], and hydrothermal approach [41]. In terms of chemistry, co-precipitation seems to be basic, however the particle size specificity is very limited [40]. High temperatures (over 600 °C) are usually needed for the ball milling process, requiring over 1000 hours to finish [38]. When compared to other techniques hydrothermal treatment seems as the best prospective technology due to its ease of use, effectiveness, and ability to modify the investigational circumstances including stirrer time, reactants, time and temperature in order to control the number of factors, including degree of agglomeration, morphology, size and content [42]. In this study, we attempted to eliminate the contamination of fluoride from the water body by utilizing hydrothermally synthesized NiO+potato peels.

Optimization and experimental design are both made easier by response surface methodology (RSM) and Box-Behnken design (BBD). This leads to greater efficiency and less waste. Because of the BBD in RSM, extended experimental runs are not needed as often, which saves a lot of time, money, and materials [43]. Industries seeking optimal circumstances with constrained resources will benefit greatly from the reduction in resource requirements. The credibility of findings is ensured by the statistical modelling which is obtained through experimental data while the precision of system representation is improved by the non-linear interaction analysis. Researchers are helped in understanding complex factor interactions by the visualization of results in the form of response surfaces and contour plots. The flexibility of the BBD inside the RSM framework allows it to be optimized in many scenarios and sectors by accommodating diverse experimental configurations. Overall, researchers may save time and energy by combining the BBD and RSM, which improves experimental operations and allows them to learn more about complex systems with less effort.

Therefore, this study aims to develop, characterize, and evaluate a novel, cost-effective adsorbent for the efficient removal of fluoride from water. The specific objectives were to: (1) synthesize and characterize NiO/potato peels nanocomposites via a hydrothermal method; (2) investigate the fluoride adsorption kinetics and isotherms to elucidate the underlying mechanism; (3) employ Response Surface Methodology (RSM) with a Box-Behnken Design (BBD) to optimize critical process parameters—including adsorbent dosage, pH, and contact time—for maximum fluoride removal; and (4) assess the practical applicability and reusability of the nanocomposite in treating simulated fluoride-contaminated water.

2. Materials and methods

2.1. Materials

Sodium hydroxide (NaOH), Nickel chloride ($NiCl_2.6H_2O$), DI water and potato peels extract were used as starting materials after stochiometric calculations following the balanced chemical equation given below.

$$NiCl_2.6H_2O + H_2O + 2NaOH\ Ni(OH)_2 + 2NaCl\ Ni(OH)_2\ NiO + H_2O$$

2.2. Synthesis of NiO/potato peels composites

A weighted quantity of nickel chloride (Sigma Aldrich, 99%) was dissolved in 50 ml of DI water while being stirred. Nickel chloride solution was continuously stirred while a dropwise addition of NaOH (Sigma Aldrich, 99%) solution was added. For the production of NiO+potato peel composites, 0 ml (S1), 10 ml (S2), 20 ml (S3), and 30 ml (S4) of the potato peel extract were utilized as well (Table 1). After one hour of stirring to ensure homogeneity, the mixed solution was put into a Teflon-lined stainless steel autoclave, and kept at 180 °C for six hours. The sodium chloride is involved in the precipitate that was generated during the hydrothermal reaction, deionized water washing was done

Table 1
Measurement of chemicals.

Sample no.	Sample name	Chemical	Quantity
S1	NiO	$NiCl_2.6H_2O$	2.37 g/mol
		NaOH	0.79 g
S2	NiO/Potato Peels 10ml	$NiCl_2.6H_2O$	2.37 g
		NaOH	0.79 g
		Potato Peels extract	10 ml
S3	NiO/Potato Peels 20ml	$NiCl_2.6H_2O$	2.37 g
		NaOH	0.79 g
		Potato Peels extract	20 ml
S4	NiO/Potato Peels 30ml	$NiCl_2.6H_2O$	2.37 g
		NaOH	0.79 g
		Potato Peels extract	30 ml

multiple times to remove this sodium chloride. To get the powder, the samples were subsequently dried for six hours at 90 °C in an oven. The sample was crushed up and placed in a bullet box for further analysis after removing all the moisture from the samples. The same method was used to create samples S2, S3, and S4, however different amounts of potato peels were added to the previous predecessors. A schematic process for the synthesis of NiO/potato peels composites has been described in Fig. 1. A variety of experimental techniques, including XRD, SEM, FTIR, and also fluoride adsorption tests, were used to examine these materials after synthesis.

2.3. Statistical method

When it comes to finding the best possible combinations of variables to obtain desired results, the RSM is an excellent empirical technique. A particular set of methods called the BBD is employed by the RSM. Here, the result is affected by three separate factors: dosage, pH, and time. To prove that this tactic works, we'll use these variables. For every one of these parameters, the experiments were run for three levels including -1, 0, and +1. In the end, with help of RSM, we achieved the goals through the appreciated insights to produce a feasible solutions for our unique circumstances. It is useful for finding the sweet spot when all the parameters work together to get the best possible result.

2.4. Batch adsorption experiments

2.4.1. Optimization of variables

Batch adsorption experiments were performed to obtain equilibrium data. A series of 50 mL test tubes containing F^- solutions were agitated at 200 rpm in a rotary shaker, maintaining a constant temperature of 25 ± 0.1 °C. After a predetermined contact time, aliquots were withdrawn using syringes and filtered through a 0.22 μm membrane. The resulting filtrates were analyzed for residual total fluoride concentration. The adsorption capacity at equilibrium, q_e (mg/g), was calculated [44] using the following mass balance equation: $q_e = (C_0 - C_e)V/m$

where C_0 and C_e are the initial and equilibrium concentrations of fluoride (mg/L), respectively, V is the volume of the aqueous solution (L), and m is the mass of the adsorbent (g).

2.4.2. Kinetic studies

Adsorption kinetics were investigated by introducing an adsorbent dosage of 1 g/L into 25 mL of fluoride solution with an initial concentration of 15 mg/L at pH 7.0. The mixtures were agitated, and samples were collected at specified time intervals. The samples were then filtered, and the fluoride concentration was quantified to track the uptake over time.

2.4.3. Effect of pH

The influence of solution pH on As(III) adsorption was evaluated across a pH range of 2 to 12. The pH was adjusted using 1 M HCl or NaOH solutions. These experiments were performed with an initial fluoride concentration of 15 mg/L and a contact time of 8 hours.

2.4.4. Effect of co-existing ions

The potential interference of common anions—including sulfate (SO_4^{2-}), chloride (Cl^-), nitrate (NO_3^-), carbonate (CO_3^{2-}), phosphate (PO_4^{3-}), and bicarbonate (HCO_3^-)—on fluoride removal was investigated under optimal adsorption conditions.

Furthermore, adsorption tests were conducted under simulated real-water conditions using a complex matrix containing 200 mg/L of SO_4^{2-} and Cl^-, 50 mg/L of NO_3^-, 10 mg/L of CO_3^{2-}, and 15 mg/L of fluoride at an initial pH of 7.0. The concentrations of these co-existing anions were selected based on their maximum contamination levels as defined by the WHO and the U.S. Environmental Protection Agency.

3. Results and discussion

3.1. X-ray diffraction analysis

The material crystal structure that has been synthesized was investigated through X-ray diffraction. The NiO with potato peels composite were predicted using diffraction peaks in the XRD. At a 2θ angle, the

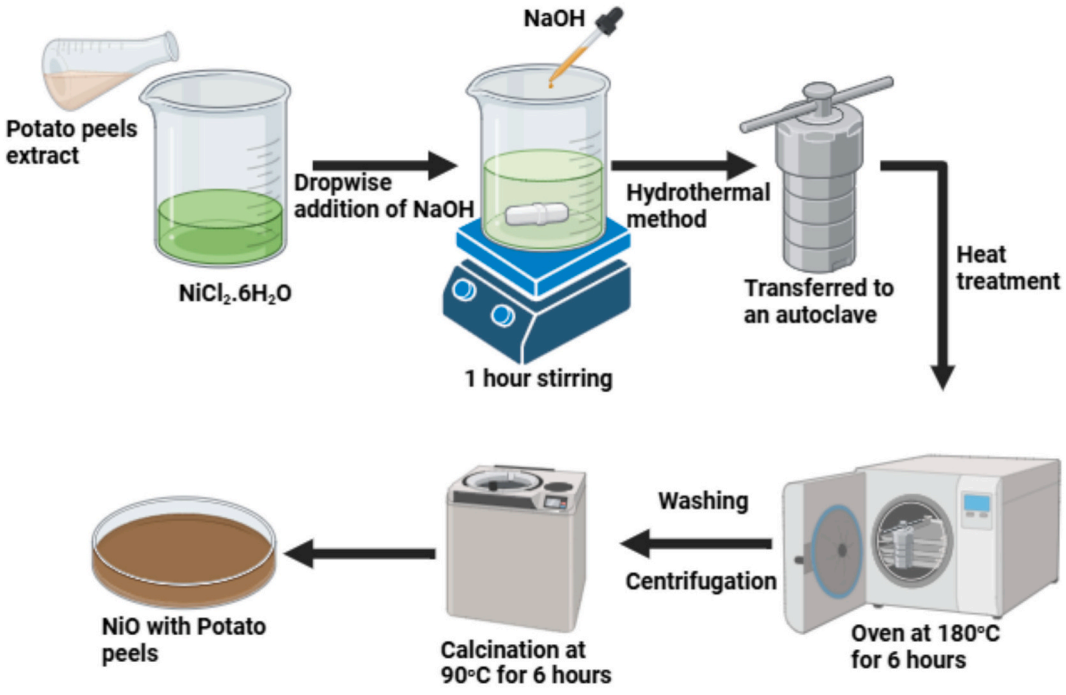

Fig. 1. Schematic representation for the synthesis of NiO with Potato peels via hydrothermal method.

diffracted intensities were seen from 20° to 80°. The crystallinity of the NiO nanoparticles (NPs) has been shown by the discovered reflections in Fig. 2. The Bragg reflections are indexed as hkl values: (130), (100), (101), (103), (110) and (001). All of the samples' diffraction peaks displayed the distinctive characteristics of a phase-pure NiO structure (Fig. 3), with the highest intensity peak coming from the (101) plane and matching the XRD data for pure nickel oxide. Because of the face-centered cubic (FCC) crystalline structure of NiO, all of these diffraction peaks may be precisely indexed to it. Their characteristic peaks' relative intensity, which is in line with the spectrum's standard value (JCPDS, No. 04-0835), is similar. Only the characteristic diffraction peaks of the FCC phase NiO were detected, indicating that the samples are single-phase, according to the XRD pattern. The diffraction peaks of nickel oxide nano powders are slightly shifted, confirming the alteration in crystal parameters but high purity of the NiO NPs prepared using the described method. For nickel oxide, nickel oxide /10ml potato peels, nickel oxide /20ml potato peels, and nickel oxide /30ml potato peels, different structural parameters are evaluated as follows;

3.1.1. Lattice constant (a)

The lattice constant (a) was estimated through the following expression [45].

$$d = \frac{a}{\sqrt{h^2 + k^2 + l^2}} \quad (1)$$

where the miller indices are denoted by (hkl) and the inter-planar spacing by (d). A decrease in the lattice constant (a) to 8.36Å, 8.38Å, 8.37Å and 8.33Å obtained is illustrated in Table 2. This slight change was observed due to addition of the potato peel into NiO.

3.1.2. Crystallite size (D)

The highest intensity diffraction peak (101) and crystallite size of these nanoparticles was determined by using Scherrer formula given as below [46].

$$D = \frac{0.9\lambda}{\beta\cos\theta} \quad (2)$$

Table 2 shows that crystalline size is decreased by increasing the quantity of potato peels extract which might be due to encapsulation of the extract around the NiO nanoparticles.

3.1.3. Unit cell volume (V)

Employing the following relationship, the volume of unit cell was assessed using lattice parameter [47].

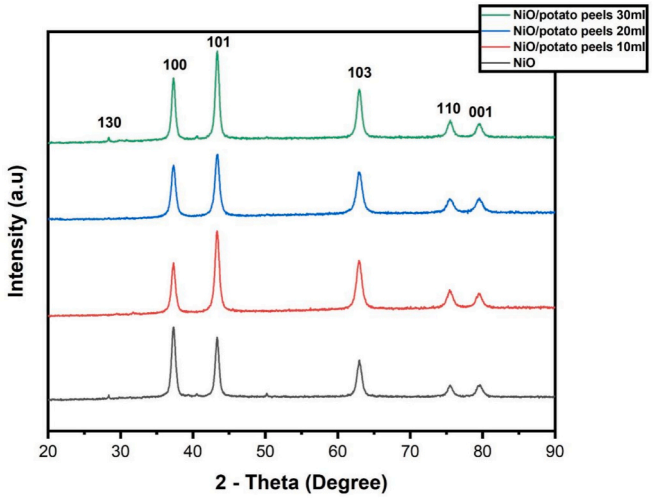

Fig. 2. XRD patterns for NiO and NiO with (10ml + 20ml + 30ml) potato peels extract.

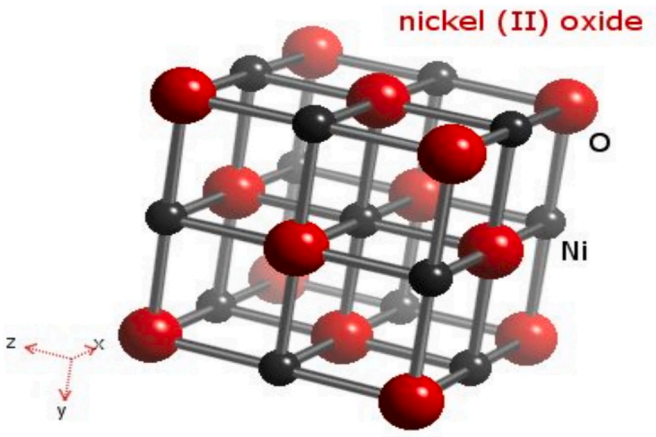

Fig. 3. Schematic diagram for Ni-O atomic distances [1]

Table 2
Variability in the structural parameters

Samples	a (Å)	V (Å^3)	D_x (g/cm^3)	D (nm)	δ (Lines/m^2)	ϵ (%)
S1	8.36	584.22	5.77	16.5	0.0249	0.249
S2	8.38	588.48	5.92	16.1	0.0225	0.258
S3	8.37	586.37	6.11	15.9	0.0372	0.384
S4	8.33	578.00	6.26	15.3	0.0315	0.368

$$V = a^3 \quad (3)$$

By the addition of potato peels, the unit cell volume is decreased (Table 2)

3.1.4. X-ray density (D_X)

Using equation below, the prepared material X-ray densities were determined [48].

$$D_x = \frac{8M}{N_A a^3} \quad (4)$$

X-ray density increased from 5.77, 5.92, 6.11 and 6.26g/cm^3. The porous nature of the extract can cause this increase in X-ray density [41].

3.1.5. Lattice strain (%)

The lattice strain was calculated with following formula [49] as a function of varying potato peels contents.

$$\varepsilon = \frac{\beta}{4\tan\theta} \quad (5)$$

"θ" denotes the Bragg's angle while "β" belongs to full width half maxima

3.1.6. Dislocation density (δ)

The dislocation density (δ) was evaluated by the crystallite size and its formula is given as below [50].

$$\delta = \frac{15\varepsilon}{aD} \quad (6)$$

In this expression, ε, D and a indicate lattice strain, crystallite size and lattice constant respectively. The increase in the quantity of potato peels enhances their values (Table 2)

3.1.7. Parameters for position of atoms and ions

The formulas given in the equations (S1-S11) were employed to calculate further structural elements for octahedral and tetrahedral locations [51] for all the samples (Table 3). The anions-cations and

Table 3
Change in positional parameters for tetrahedral and octahedral sites for NiO/potato peels extract.

x	a (A°)	r_A (A°)	r_B (A°)	R_A (A°)	R_B (A°)	L_A (A°)	L_B (A°)	d_{AL} (A°)	d_{BL} (A°)	d_{ALE} (A°)	d_{BLE} (A°)	d_{BLEU} (A°)
S1	0.42	0.56	0.71	1.95	2.02	2.98	3.64	1.91	2.06	3.12	2.81	2.98
S2	0.34	0.54	0.69	1.93	2.01	2.95	3.61	1.89	2.04	3.09	2.79	2.95
S3	0.27	0.52	0.67	1.91	2.00	2.93	3.58	1.87	2.02	3.06	2.77	2.92
S4	0.24	0.50	0.65	1.89	1.99	2.90	3.55	1.85	2.00	3.03	2.75	2.89

interstitials distances at A and B locations (R_A & R_B) were calculated by using following formulae, the anion-cation spacing loop lengths (L_A& L_B), A and B sites length (d_{BL} and d_{AL}), also the shared edge lengths of the octahedron and tetrahedron (d_{ALE} & d_{BLE}).

3.1.8. Interionic distances

The equations S12-S18 are used to compute the Ni-O lengths (p, q, r, and s) and the Ni-Ni distances (between cations, i.e., b, c, d, e, and f) [52]. The calculated values for all these parameters are listed in Table 4. It can be observed from Table 4 that there is a slight variation in these parameters which is definitely due to a slight change in the value of lattice parameter as discussed above.

3.2. Fourier transform infrared spectroscopy (FTIR)

As an illustration of the functional groups analysis, Fourier Transforms Infrared spectra of NiO also NiO with potato peels composite are displayed in Fig. 4. Fourier Transforms Infrared spectra of NiO range between 400 & 4000 cm^{-1}. The spinel structure of generated samples is verified through two notable absorption peaks within the range of 400–600 cm^{-1} region. The stretching vibration for octahedral and tetrahedral metal oxygen bonds be accountable for absorption bands seen at 665 cm^{-1} & 543 cm^{-1}, respectively [53]. Another group observed that the vibration at roughly 1245 cm^{-1} was the result by O-H bending [54,55]. A region showing a water bond is found between 2900 and 3400 cm^{-1}. The peak that appears at 3126 cm^{-1} represents the O-H stretching vibrational modes of water (H_2O). A peak near 1087 cm^{-1} due to C-O adsorption indicates the vibration modes of the C-O group band [56]. Due to comparable characteristic absorption peaks, these data imply the existence of organic chemicals in the sample in addition to the new inorganic substance (Ni-O). This result is consistent with earlier research in the literature. Finally, the emergence of absorption bands at 485 cm^{-1} provides evidence for the production of NiO nanoparticles by confirming the existence of stretching vibrations linked to the Ni-O bonds [57,58].

3.3. Scanning electron microscopy

The scanning electron microscopy (SEM) was utilized to identify the grain size and morphology of the prepare material. SEM images of NiO (*Fig.* 5) and NiO accompanying vegetable peels (*Fig.* 5) tell that the resulting samples contain clusters of nanoparticles. The SEM images apparently show a kind of piece size and non-uniform shape. The SEM images determine a more apparent view of the piece accumulation. Carelessly scattered potato peels pieces of various sizes may be observed alongside the coat with metallic material group of chemical elements atoms. The microstructure resides of a single type of piece, signifying the

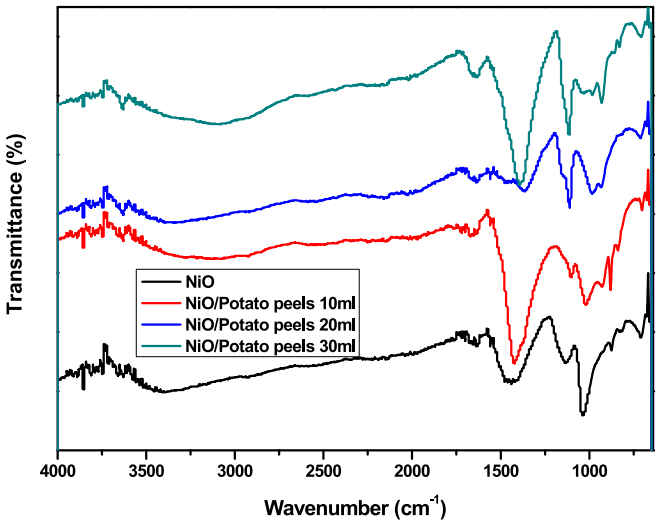

Fig. 4. Fourier transform infrared spectra (FTIR) for NiO and NiO with (10ml + 20ml + 30ml) potato peels extract.

deficiency of any supplementary subordinate chapters. By employing foul line interrupt method, the average grain proportion for NiO and NiO/potato peels was observed to be between 80nm to 91 nm (Table 5), individually. As an alone seed consists of diversified crystallites, the size of grain of every sample, established by Scherrer rule, is more the crystallite size. Furthermore, it has been observed that the addition of peels extract causes to reduce the grain size and acts as grain inhibitor [33].

3.4. Adsorption studies

3.4.1. Zeta potential measurements

It has long been considered that the adsorbents' pH_{PZC} (pH point of zero charge) is related to the impact of pH on fluoride adsorption [59]. Thus, zeta potential changes at various pH values and fluoride adsorption at primary fluoride concentration of 10 mgL^{-1} were studied, the findings are displayed in Fig. (6a & 6b). The nickel oxides have an external surface covered in OH functional groups and are fully hydrated in water [60,61]. The adsorbent surface might experience protonation or deprotonation depending on the pH value, resulting in the development of basic or acidic properties, accordingly. Succeeding chemical equations could be utilized to clarify these reactions.

Heavy metal ions and the iron oxide surface interact electrostatically as a result of the aforementioned reactions. Fig. (6a & 6b) illustrates how

Table 4
Inter-ionic distances (p, q, r, s, b, c, d, e, f) for all samples.

x	p (± 0.01)	q (± 0.01)	r (± 0.01)	s (± 0.01)	b (± 0.01)	C (± 0.01)	d (± 0.01)	e (± 0.01)	f (± 0.01)
S1	2.071	1.934	4.262	3.693	3.009	3.581	3.681	5.530	5.213
S2	2.050	1.911	4.142	3.682	2.990	3.562	3.662	5.494	5.128
S3	2.041	1.892	3.712	3.655	2.962	3.538	3.638	5.456	5.145
S4	2.040	1.873	3.590	3.632	2.944	3.408	3.608	5.413	5.105

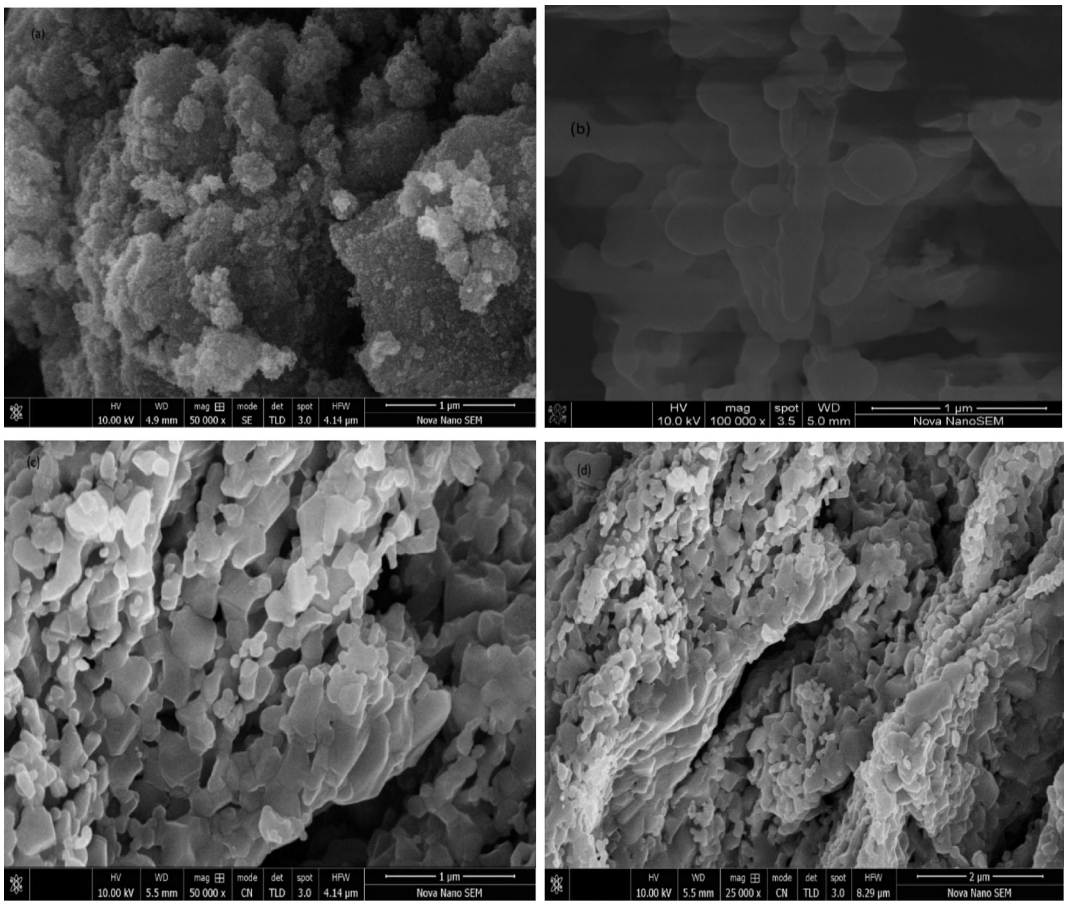

Fig. 5. SEM micrographs of (a) NiO (b) NiO/ Potato Peels (10ml), (c) NiO/Potato Peels (20ml), NiO/Potato Peels (30ml).

Table 5
Sample grain size for different samples.

Sample No	Material	Size
S1	NiO	91.0 nm
S2	NiO/Potato Peels (10ml)	80.4 nm
S3	NiO/Potato Peels (20ml)	85.6 nm
S4	NiO/Potato Peels (30ml)	82.9 nm

the zeta potential for the NiO and NiO+20ml potato peels varies with pH. It can be found that the values of zeta potential decreased with pH values [62]. The adsorbent surface is negatively charged above pH_{PZC}, and it most likely draws positively charged ions (cations). On the other hand, the adsorbent's positively charged surface draws negatively charged ions (anions) below pH_{PZC}. Notably, the pHpzc values for the NiO and NiO+20ml potato peels were 8.0.

3.4.2. *Effect of pH*

The adsorbent surface charge and rate of adsorbate speciation and ionization are influenced by the pH, it is crucial in the absorption of metal ions [63]. It is evident in Fig. (6a & 6b) that the adsorption procedure for both materials was highly reliant on the solution's initial pH value. Fluoride absorption increased when the pH range was below 6 (Fig. 6a) because the adsorbent material was positively charged. Fig. 6b illustrates a minor drop in adsorption as the pH range relies below 5. The elimination of fluoride was stabilized while the pH was between 6 and 8. Fluoride removal decreased as the pH level above 10 because the adsorbent material became negatively charged. We can therefore determine that fluoride adsorption entailed electrostatic interaction as well. On the basis of obtained results, it can be affirmed that NiO with potato peels extract can be effectively utilized as suitable adsorbents to remove the fluoride ions from the polluted water since the pH of natural water is determined to be approximately 7.

3.4.3. *Effect of contact time*

The effectiveness of removing contaminants from aqueous solutions and the interaction between the adsorbent and adsorbate species are significantly influenced by the contact time. The removal of fluoride from water over time is seen in Fig. (6c). The study's findings are presented following [64]. The Fig. illustrates how fluoride removal rises with increasing time. Results indicated that fluoride was eliminated with increasing contact times from (0 to 180 minutes). the maximum amount of fluoride (94.70%) was eliminated in the first 180 minutes. Most fluoride is eliminated within 180-360 minutes, and highest at 360 minutes and remaining constant after that. The initial moments of an adsorption process showed an excellent adsorption rate because of the availability of active sites and the minor fluoride content at the adsorbent's surface.

Understanding the mechanism of fluoride sorption on NiO with potato peels is frequently aided by considering kinetics. The mechanism of adsorption was investigated by testing the adsorption kinetics data utilizing the pseudo-first-order and pseudo-second-order models. The expressions for the PFO & PSO models are given below [11].

$$\ln(q_e - q_t) = \ln q_e - \frac{K_1}{2.303}t \tag{7}$$

$$\frac{t}{q_t} = \frac{1}{K_2 q_e^2} + \frac{1}{q_e}t \tag{8}$$

(K_1) (PFO) rate constant, (K_2) (PSO) rate constant and (q_t) adsorption capacity. The linear plot characteristic of ln (q_e– q_t) vs time t at different

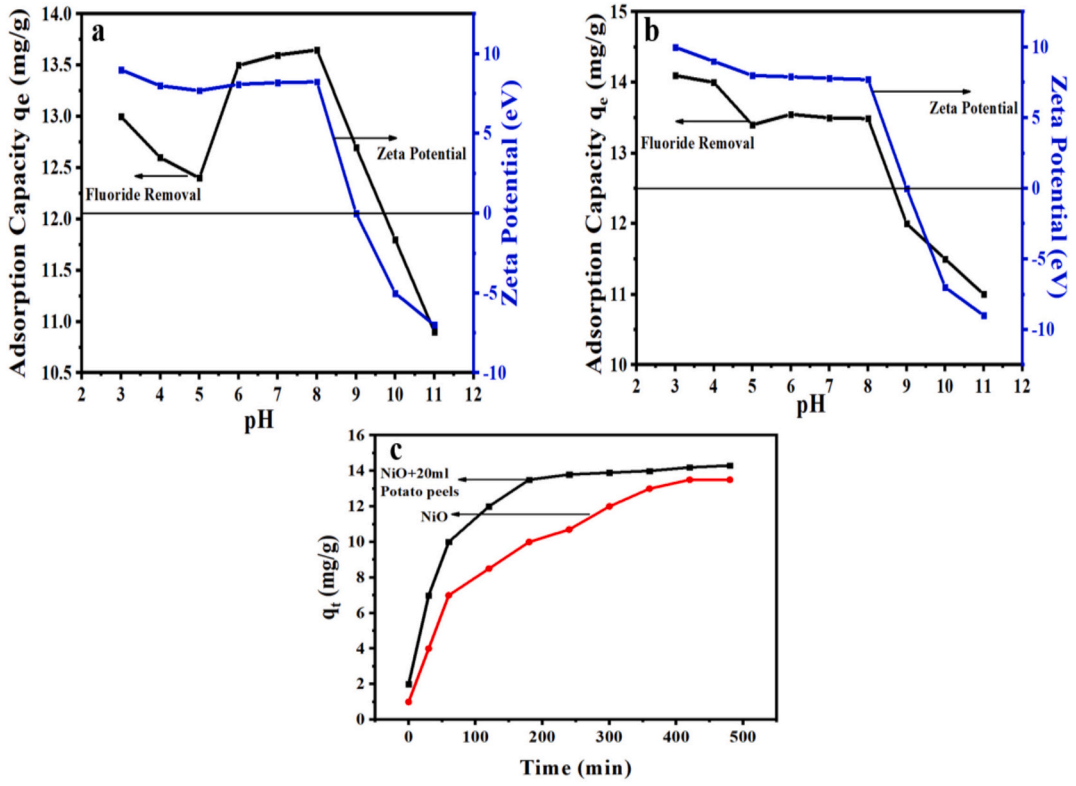

Fig. 6. The change in zeta potential with respect to various pH values for **(a)** NiO **(b)** NiO + 20ml potato peels extract. **(c)** Effect of contact time on fluoride removal.

initial fluoride concentrations is derived for the PFO kinetics model (Fig. 7a). The linear plot characteristic of t/q_t vs time t at different initial fluoride levels is derived for the pseudo-second-order kinetics model (Fig. 7b). Kinetic parameters for PFO and PSO, including q_e, k_1, k_2, and R_2, were determined using these graphs and are presented in Table 6. R^2 was less than 0.90, indicating poor linearity in the PFO plot. However, PSO (R^2 >0.99) demonstrated strong linearity and best fit to the experimental results. Additionally, there was a similarity between the pseudo-second-order model estimated values (q_e, cal.) and investigational data (q_e, exp.). Moreover, the PSO model's R^2 values are extremely near to 1, indicating how pseudo-second-order model offers a more accurate fitting for the kinetics data of fluoride ions adsorption onto NiO+potato peels than the PFO model. Furthermore, the best fitting of PSO model with experimental data confirms that the adsorption is chemisorption [10]. The applicability of the PSO kinetic model demonstrated that the two binding centers are involved in the adsorption of metal ion on adsorbents [65].

3.4.4. *Co-existing anions effects*

Because of the complex structure of both surface and ground water, other ions Cl^-, NO_3^{-1}, CO_3^{-2} PO_4^{-3}, SO_4^{-2}, and HCO^{-3} may be present in the water body. The efficiency of the adsorbent under investigation may suffer as a result of these ions' possibility to contend with fluoride for accessible sites that are active for adsorption on the surface of NiO and NiO + potato peels. Fig. (8a & 8b) illustrates how coexisting anions affect fluoride removal at various concentrations. The findings showed that Cl^-, NO_3^{-1}, and CO_3^{-2} had negligible impacts on the elimination of fluoride. When ($PO4^{-3}$, SO_4^{-2}, and HCO^{-3}) existed in concentrations more than 0.50mM, there was a noticeable reduction in the quantity of fluoride ions eliminated. A decrease in fluoride removal (%) as in the

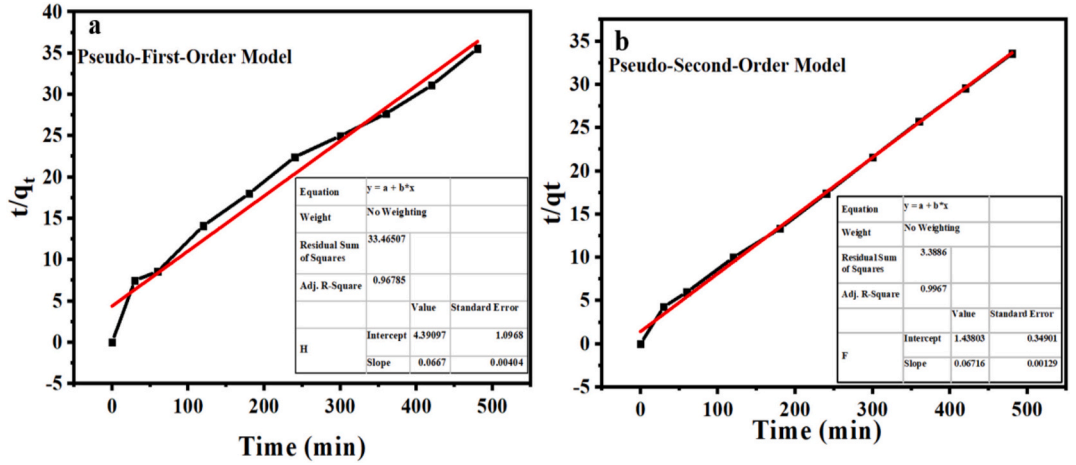

Fig. 7. Adsorption kinetics (a) Pseudo-First-Order (PFO) (b) Pseudo-Second-Order (PSO) kinetics models.

Table 6
Details about adsorption kinetics.

Adsorption kinetics	Equations	Fluoride adsorption parameters
Pseudo first order	$\ln(q_e - q_t) = \ln q_e - \frac{K_1}{2.303}t$	q_e=4.39097, k_1=0.0667, R^2=0.96785
Pseudo second order	$\frac{t}{q_t} = \frac{1}{K_2 q_e^2} + \frac{1}{q_e}t$	q_e=1.43803, k_1=0.06716, R^2=0.9967

existence of ($PO4^{-3}$, SO_4^{-2}, and HCO^{-3}) is the cause of the competition ions from an active sorption site on the adsorbent's surface [66]. The ratio of charge to radius of coexisting anions is highly influenced by the degree of fluoride removal. Adsorbent and anions have a higher binding affinity when the charge/radius ratio values rise. Since the layout of anions decreases with radius or charge as $HCO^{-3} > SO_4^{-2} > PO_4^{-3} > NO_3^{-1} > CO_3^{-2} > Cl^-$, the interference of PO_4^{-3}, SO_4^{-2}, and HCO^{-3} ions has a higher percentage effect on the ions that remove fluoride.

3.4.5. Regeneration study

We carried out a five-cycle experiment to look into stability and reusability of the NiO and NiO + potato peels as adsorbents. Fig. (9a & 9b) illustrates the removal of fluoride for several regeneration cycles at initial concentrations of 15 mg/L. Fluoride ions have been found to be eliminated from adsorbent surfaces by sodium hydroxide (NaOH) hydroxyl exchange in alkaline solution. Additionally, the desorption process is significantly influenced by electrostatic repulsion. The NiO+potato peels ability to adsorb and desorb fluoride was assessed over a period of five consecutive cycles. Following five consecutive cycles, the fluoride concentration in the effluent met the WHO-approved standard, and adsorption capacity of the NiO & NiO + potato peels was 14.86 mg/g which quickly dropped to 10 mg/g in the case of NiO. This demonstrated that NiO+potato peels can be employed as a fluoride adsorbent in a variety of sequential cycles.

3.4.6. Comparison study of the adsorption capabilities of fluoride

Efficacy of eliminating fluoride through NiO+potato peels was assessed in contrast to the various adsorbents suggested by researchers. The outcomes show that using NiO with potato peels effectively removes fluoride from aqueous solutions. PSO more closely corresponded with the sorption procedure, according to kinetic assessments. The quantity of fluoride ions which are eliminated from aqueous solutions is considerably influenced by pH. In general, compared to previously stated materials, NiO+potato peels have noticeably higher adsorption capacities (Table 7).

3.4.7. Environmental significance

The adsorption capacities of the NiO and NiO + potato peels extract were evaluated for use in the treatment of fluoride-contaminated water at realistically simulated conditions, with primary concentration of 15 mg/L. Fig. 10 demonstrates how the fluoride content of the simulated water specimen steadily drops as treatment interval increases. The concentration of fluoride in the NiO with (10 ml + 20 ml + 30 ml) potato peel extract was significantly lower than that of NiO. After just two hours, the content of fluoride surface was below 1.5 mg/L, which complied with an aqueous medium limit contains fluoride (F^{-1}) specified by World Health Organization (WHO). Within two hours of adsorption, the amount of fluoride ions stabilized, demonstrating that every available site had been filled. Therefore, it makes sense to believe that NiO + potato peels will work as a very powerful adsorbent to purify water that has been polluted by fluoride.

3.4.8. Proposed adsorption mechanism

The exceptional fluoride adsorption performance of the NiO/Solanum Tuberosum peels nanocomposite is attributed to a synergistic interplay of several mechanisms. The experimental data from zeta potential, kinetics, and FTIR analyses collectively point towards a process dominated by chemisorption via ligand exchange, complemented by electrostatic interaction and the enhanced surface properties provided by the bio-support.

3.4.8.1. Dominant role of electrostatic attraction and surface charge. The initial interaction between the fluoride ions (F^-) and the adsorbent surface is heavily influenced by the solution pH, as governed by the surface charge of the nanocomposite. The point of zero charge (pH_{PZC}) was determined to be approximately 8.0 for both NiO and the NiO/potato peel composite (Fig. 6a & 6b). At pH values below the pH_{PZC}, the surface hydroxyl groups (M–OH) on the NiO nanoparticles become protonated, resulting in a positively charged surface ($M–OH_2^+$). This positively charged surface creates a strong electrostatic attraction for the negatively charged fluoride anions, facilitating their initial migration from the bulk solution to the adsorbent surface. This explains the high removal efficiency observed in the acidic to neutral pH range (Fig. 6a & 6b). As the pH increases beyond the pH_{PZC}, the surface becomes negatively charged ($M–O^-$), leading to electrostatic repulsion of F^- ions and a consequent decrease in adsorption capacity.

3.4.8.2. Chemisorption via ligand exchange as the primary mechanism. While electrostatic attraction is crucial for the initial uptake, the adsorption data strongly indicates that a more specific and stronger chemisorption process is the primary mechanism. This is conclusively demonstrated by the superior fit of the kinetic data to the Pseudo-Second-Order (PSO) model ($R^2 > 0.99$, Table 6). The PSO model is

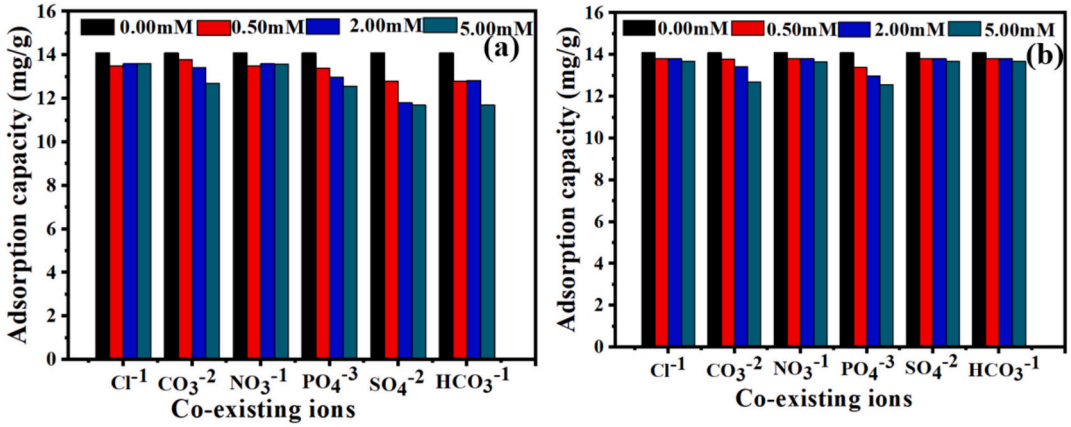

Fig. 8. The impact of several coexisting ions on the adsorption capability of **(a)** NiO **(b)** NiO + 20ml potato peels extract.

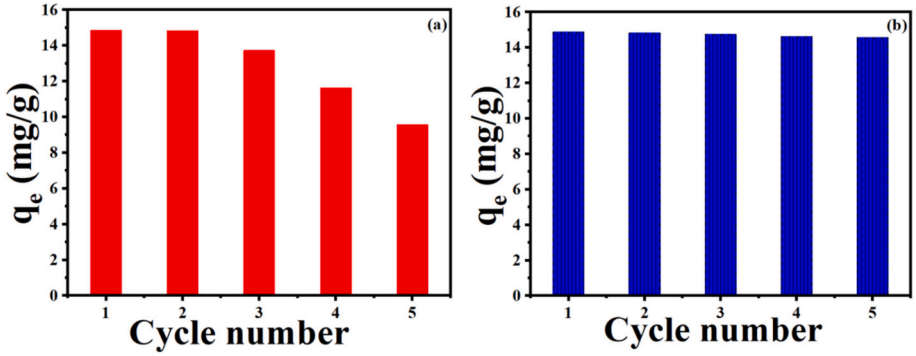

Fig. 9. Regeneration test of the adsorbents of **(a)** NiO **(b)** NiO + 20ml potato peels extract.

Table 7
Comparison of adsorption capacity of previously reported adsorbents with the adsorbent in the present study.

Adsorbents	pH	Adsorption (mg/g)	References
Metallurgical-grade alumina	5.0-6.0	12.57	[57]
Manganese oxide modified activated alumina	5.5	10.18	[58]
Iron (III)-tin (IV) mixed oxide	6.4	10.47	[59]
Treated biogenic apatite	6.0	6.84	[60]
Cellulose/HAP composite	5.0	4.18	[61]
Aligned carbon nanotubes (CNTs)	7.0	4.5	[62]
Acid–base treated raw laterite (TL)	5.0	11.8	[63]
NiO + Potato peels	6.0-8.0	13.5	This study

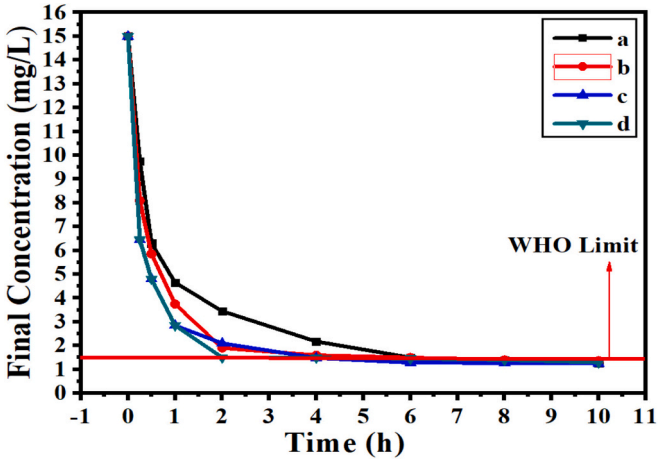

Fig. 10. Fluoride concentration for simulated real water samples based on treatment time for **(a)** NiO **(b)** NiO + 10ml potato peels extract **(c)** NiO + 20ml potato peels extract **(d)** NiO + 30ml potato peels extract.

based on the assumption that the rate-limiting step is a chemical reaction involving valence forces through the sharing or exchange of electrons between the adsorbent and adsorbate.

In this context, we propose that the dominant chemisorption mechanism is ligand exchange (or surface complexation), where the fluoride ions directly replace the hydroxyl groups on the surface of the NiO nanoparticles, forming strong inner-sphere complexes: This bond formation is characteristic of chemisorption and accounts for the high adsorption capacity and the strong agreement with the PSO model. The slight shifts or changes in the FTIR spectra (Fig. 4), particularly in the regions associated with metal-oxygen (Ni–O) and O–H stretching/bending vibrations after fluoride adsorption, provide further evidence for this surface complexation, suggesting a direct chemical interaction between F^- and the NiO surface sites.

3.4.8.3. Synergistic contribution of the potato peel bio-support. The potato peel matrix is not merely an inert support but plays an active and synergistic role in enhancing the adsorption process. Its contribution is threefold: (i) The porous structure of the carbonaceous potato peel biomass (as inferred from SEM analysis) provides a high surface area and a scaffold that prevents the agglomeration of NiO nanoparticles. This maximizes the exposure of active NiO sites and facilitates the diffusion of fluoride ions to these sites. (ii) The potato peel itself contains various oxygen-containing functional groups (e.g., carboxyl -COOH, hydroxyl -OH, as indicated by the FTIR peaks at ~3126 cm^{-1} and ~1087 cm^{-1}). These groups can participate in the adsorption process through hydrogen bonding with fluoride ions or weak electrostatic interactions, providing secondary adsorption sites that complement the primary chemisorption on NiO. (iii) The integration with the biomass improves the dispersion of NiO nanoparticles in the aqueous solution, increasing the accessibility of active sites and thereby boosting the overall kinetics and efficiency of fluoride removal.

3.4.8.4. Interference from co-existing anions. The influence of co-existing anions (Fig. 8a & 8b) further validates the proposed mechanisms. Anions with a higher charge density (e.g., PO_4^{3-}, SO_4^{2-}, HCO_3^-) competed more significantly with F^- for adsorption sites. This competition is most acute for the specific chemisorption sites involved in ligand exchange, as these multivalent anions also have a strong affinity to form inner-sphere complexes with the metal oxide surface. The lesser interference from monovalent ions like Cl^- and NO_3^- confirms that non-specific electrostatic attraction plays a secondary role, as these ions would be expected to compete more strongly if that were the dominant mechanism.

In summary, the fluoride adsorption onto the NiO/potato peel nanocomposite is a multi-mechanistic process initiated by electrostatic attraction, which is most favorable at pH < pH_{PZC}. This is rapidly followed by the primary and rate-controlling step of chemisorption via ligand exchange, where F^- ions form strong inner-sphere complexes with the surface Ni atoms. The potato peel bio-support acts synergistically by providing a high-surface-area, functionalized matrix that enhances nanoparticle dispersion and offers supplementary adsorption sites. This comprehensive mechanism explains the high efficiency, rapid kinetics, and strong binding affinity observed, positioning the synthesized nanocomposite as a highly effective and sustainable adsorbent for water defluoridation.

3.5. Analysis of the Box-Behnken design

3.5.1. Analysis of variance (ANOVA)

In Table 8, you can see the RSM analysis's design and findings, as well as the coefficients that came from the adsorption capacity tests. The

Table 8
Design and performance of RSM for fluoride adsorption with NiO/Solanum Tuberosum peels nanocomposites.

Run Order	Factor 1 A: Dose g/L	Factor 2B: pH	Factor 3 C: Time min	Actual Value q_e mg/g	Predicted Value q_e mg/g	Residual	Leverage	Internally Studentized Residuals	Externally Studentized Residuals
1	1	11	242.5	10.5	10.18	0.3250	0.750	0.726	0.653
2	0.75	3	480	12.5	12.64	-0.1375	0.750	-0.307	-0.255
3	1	7	5	1.2	1.66	-0.4625	0.750	-1.034	-1.052
4	0.5	11	242.5	6.3	7.00	-0.7000	0.750	-1.564	-2.976
5	1	3	242.5	13.6	12.90	0.7000	0.750	1.564	2.976
6	0.5	7	480	8.5	8.04	0.4625	0.750	1.034	1.052
7	0.5	3	242.5	8.1	8.43	-0.3250	0.750	-0.726	-0.653
8	0.75	7	242.5	12.2	12.20	0.0000	$1.000^{(2n}$		
9	1	7	480	13.4	13.96	-0.5625	0.750	-1.257	-1.492
10	0.5	7	5	0.5	-0.0625	0.5625	0.750	1.257	1.492
11	0.75	11	5	0.5	0.3625	0.1375	0.750	0.307	0.255
12	0.75	3	5	1.5	1.74	-0.2375	0.750	-0.531	-0.455
13	0.75	11	480	10.1	9.86	0.2375	0.750	0.531	0.455

regression coefficients, which comprised a quadratic, linear model, interaction variables and intercept (Table S1), were computed using the least squares approach. A higher value of the coefficient of determination ($R^2 = 0.9923$) indicates that the experimental data is accurately represented by the second order polynomial equations (equations 9 and 10). Additional proof of the model's robustness is given by the analysis of variance (Table 9).

The model F-value of 42.85 (Table 9) indicates the model's relevance. An F-value this high could only be explained by random chance by a mere 0.52%. The terms of model are deemed substantial if the P-value is small as compared to 0.05 [67]. A, B, C, and C^2 were the significant terms of model in this case. Because it evaluates signal-to-noise ratio, Adeq Accuracy number is an essential sign to estimating the trustworthiness of model. When this value is higher than 4, a noticeable signal is generated by the model when contrasted to a background noise [68,69]. Table S2 shows 17.87 an Adeq Precision number, which is larger than 4, according to the analysis. This means that the model is more resilient and reliable. Here is the coded form of the equation for qe:

The given equation can be paraphrased as follows:

$$q_e = 12.20 + 1.91\,A - 1.04\,B + 5.10\,C - 0.3250\,AB + 1.05\,AC - 0.3500\,BC - 1.41\,A^2 - 1.16\,B^2 - 4.89\,C^2 \quad (9)$$

The equation comprises on coded factors predict much more easier answer for a specific quantity of each element. In the beginning, the factors are given the values +1 for high levels and -1 for low levels. In order to compare the factor coefficients, we can use the encoded equation and find out how important each element is. Here is the real equation:

q_e = -17.41 + 39.53 Dosage + 1.09 pH + 0.052 Time -0.32 Dosage * pH + 0.017 Dosage * Time - 0.0003 pH * Time - 22.60 $Dosage^2$ - 0.07 pH^2 - 0.00008 $Time^2$ (10)

For specific values of each factor, one can predict the result by stating an equation in reference to the actual factor. Here, we need to deliver the quantity of each element in their original unit. The predictable values predicted by equations 9 and 10 were highly concordant with the

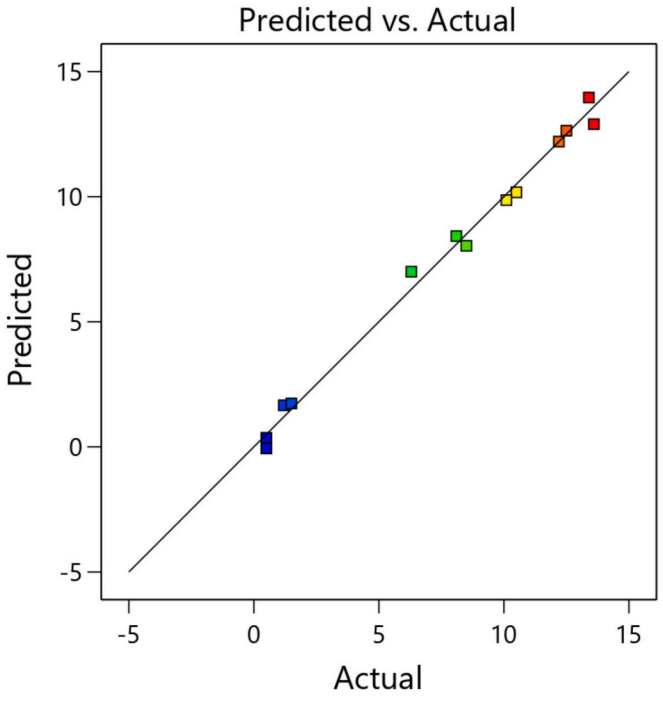

Fig. 11. Predicted versus actual value of q_e for F^- adsorption by NiO/Solanum Tuberosum peels nanocomposites.

Table 9
ANOVA parameters of RSM for the fitted model for F^- adsorption by NiO/Solanum Tuberosum peels nanocomposites.

Source	Sum of Squares	df	Mean Square	F-value	p-value	
Model	308.81	9	34.31	42.85	0.0052	significant
A-Dosage	29.26	1	29.26	36.54	0.0091	
B-pH	8.61	1	8.61	10.75	0.0465	
C-Time	208.08	1	208.08	259.83	0.0005	
AB	0.4225	1	0.4225	0.5276	0.5202	
AC	4.41	1	4.41	5.51	0.1006	
BC	0.4900	1	0.4900	0.6119	0.4911	
A^2	4.56	1	4.56	5.69	0.0971	
B^2	3.09	1	3.09	3.86	0.1443	
C^2	54.60	1	54.60	68.18	0.0037	
Residual	2.40	3	0.8008			
Cor Total	311.21	12				

experimental data displayed in Fig. 11. Therefore, the experimental technique fits well be the second degree model [67–69].

3.5.2. Plots of interferences

Each variable in the carefully measured interplanetary design is compared in the perturbation plot at a given point. Fig. S1 shows the correlation between stirring and the F^- adsorption capacity of the NiO/Solanum Tuberosum peels Nano composites. One component was varied within its fluctuation while the others were held constant in order to regulate the yield response. How each part influences a main area of the planned environment is highlighted by this story, such as pH, time, and dosage. It appears that each component improves the F^- adsorption capability of NiO/Solanum Tuberosum peels nanocomposites. The quick change in adsorption capacity in reaction to both pH and adsorption length was demonstrated by the correlation between the two variables. By comparing the coefficients in equation 10, we were able to determine which parameter was critical. The adsorption process's response to changes in length, pH level, and dosage of F^- in NiO/Solanum Tuberosum peels nanocomposites was linearly improved with time.

3.5.3. Optimizing the adsorption of F- onto NiO/Solanum tuberosum peels nanocomposites

How each parameter affected the adsorption dimensions in the experimental region under study, the response surface plots of the equation were constructed. In Fig.s 12, S2 and S3, we can see how the time, dosage, and pH affect the adsorption capacity. 2D and 3D response surface plots and contour plots are used to illustrate this relationship. The outcomes exhibited that the F- adsorption capability of NiO/Solanum Tuberosum peels nanocomposites increased with increasing pH, duration, and dosage.

3.5.4. Determining if the model is appropriate

Confirming that the fitted model faithfully depicts the real system is usually crucial within furthermost cases [70]. Without a well-fitting model, it is quite probable that the analysis and optimization will yield inaccurate or unsatisfactory results. When determining whether a model is suitable, the residual is crucial resulting as of the least squares fit [67,70]. Fig. 13a shows the result of transforming the residuals into the normal probability map, which allowed us to confirm the normalcy assumption. Which confirmed the prediction and showed a mostly linear pattern. The residuals compared to the predicted reaction are shown in Fig.s 13b and c. Assuming that the alteration of the primary observations is constant on behalf of all values of qe, the residuals seem to follow a normal distribution throughout the presentation [71–73]. By applying RSM, the adsorption process can be better understood.

3.5.5. Model validation

Examining the predicted and actual outcomes of various extraction setups is the goal of rechecking studies [67,70]. There were no statistically important alterations ($p > 0.05$) identified on behalf of the three supplied factor, indicating that RSM model was precise according to the findings of the empirical trials [74–76]. The response model successfully

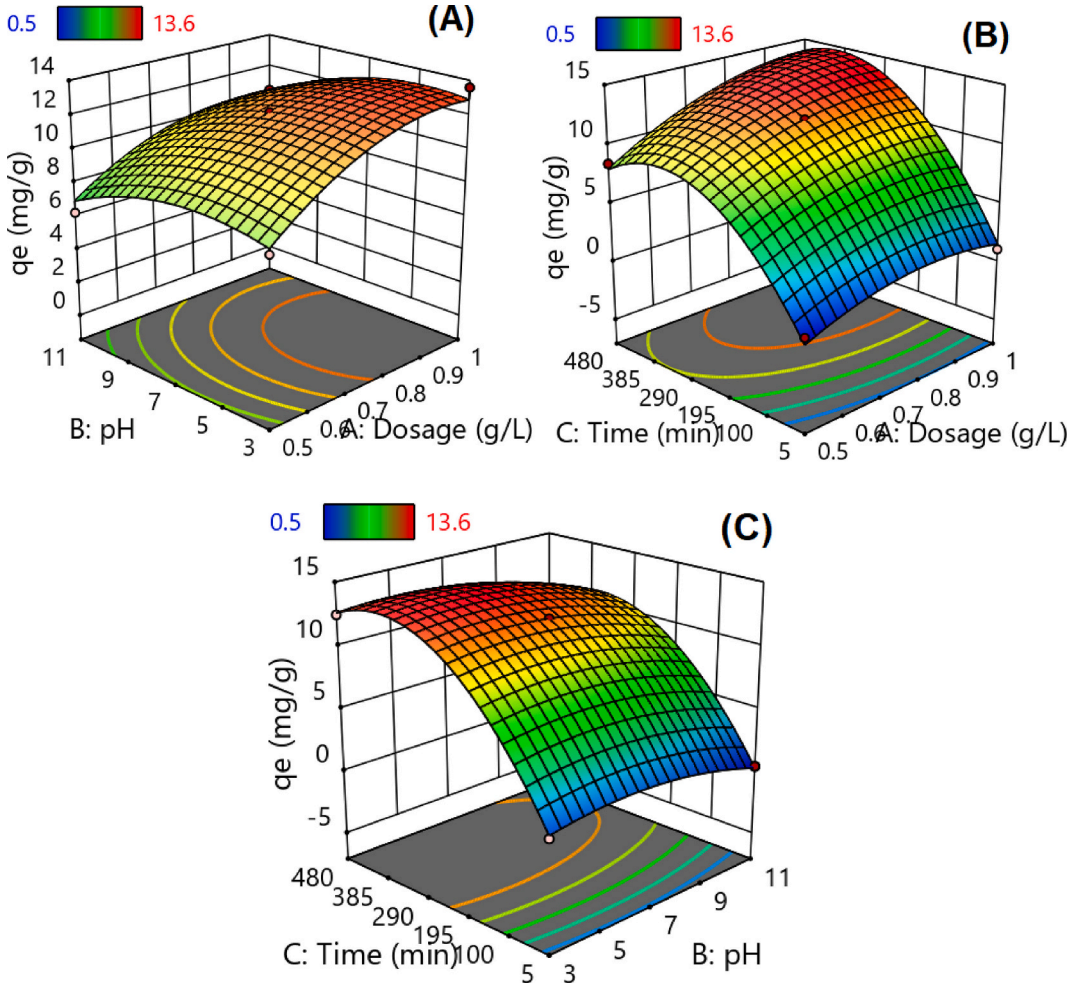

Fig. 12. Interaction effects of different factors on F^- adsorption by by NiO/Solanum Tuberosum peels nanocomposites: (a) interaction effects of pH and dosage; (b) interaction effects of time and dosage; (c) interaction effects of time and pH.

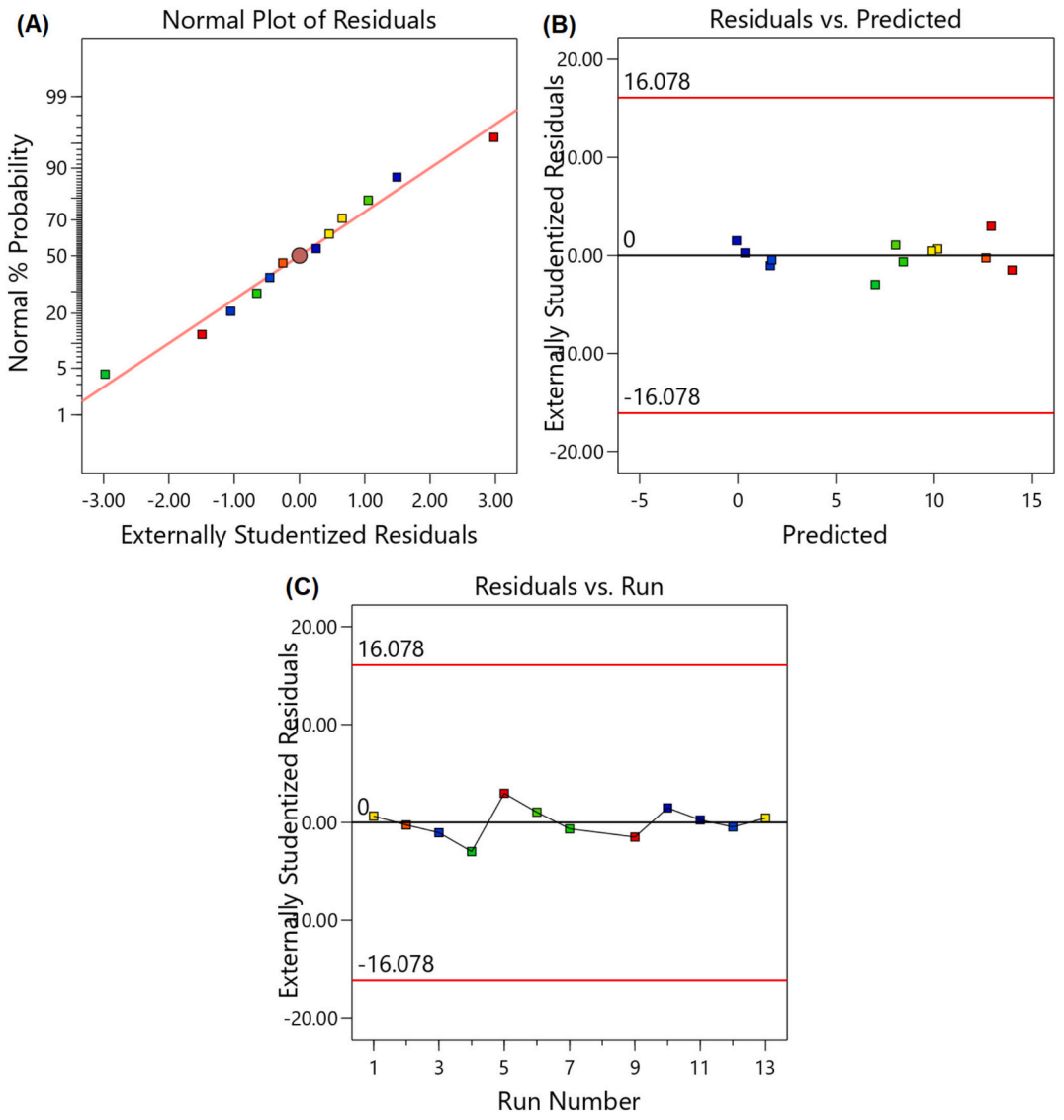

Fig. 13. Externally studentized residuals versus (a) normal % probability, (b) predicted, (c) run number for F^- adsorption by NiO/Solanum Tuberosum peels nanocomposites.

captured expected adsorption capability conditions, as shown by the durable association between the experimental and projected results.

4. Conclusion

"In conclusion, this study successfully demonstrates that the hydrothermally synthesized NiO/potato peels nanocomposite is a highly efficient and sustainable adsorbent for fluoride removal, achieving a maximum adsorption capacity of 14.86 mg/g under conditions optimized by RSM-BBD: a dosage of 1 g/L, pH of 7, and contact time of 480 minutes. The adsorption process, best fit by the pseudo-second-order model ($R^2 > 0.99$), was dominated by chemisorption, enabling the reduction of fluoride from 15 mg/L to below the WHO limit of 1.5 mg/L within just two hours. Furthermore, the nanocomposite exhibited outstanding reusability, retaining a capacity of ~14 mg/g over five cycles, confirming its potential as a robust, cost-effective, and practical solution for the remediation of fluoride-contaminated water.

CRediT authorship contribution statement

Mukhtar Ahmad: Supervision, Investigation, Conceptualization. **Khurram Shehzad:** Formal analysis, Data curation. **Ghulam Abbas Ashraf:** Project administration, Methodology, Investigation. **Muhammad Iqbal Asif:** Writing – original draft, Methodology, Investigation. **Doniyor Jumanazarov:** Formal analysis, Data curation. **Farruh Atamurotov:** Formal analysis, Data curation, Conceptualization. **Ahlem Guesmi:** Validation, Software, Methodology. **Imed Boukhris:** Data curation, Formal analysis. **Rizwan ul Hassan:** Data curation, Conceptualization.

Author statement

Mukhtar Ahmad and Rizwan ul Hassan supervised the research work, Muhammad Iqbal Asif wrote the original draft, Khurram Shehzad and Ghulam Abbas Ashraf provided the necessary experimental facilities, Doniyor Jumanazarov, Farruh Atamurotov, Imed Boukhris and Ahlem Guesmi provided the help to analyze the data using different models.

Declaration of competing interest

The authors declare that they have no known competing financial interests or personal relationships that could have appeared to influence the work reported in this paper.

Acknowledgement

The authors extend their appreciation to the Deanship of Research and Graduate Studies at King Khalid University for funding this work through the Large Research Project under grant number RGP2/376/46.

Appendix A. Supplementary data

Supplementary data to this article can be found online at https://doi.org/10.1016/j.inoche.2025.115877.

Data availability

Data will be made available on request.

References

[1] S.Y. Wang, et al., Probable causes of the abnormal ridge accompanying the 2013–2014 California drought: ENSO precursor and anthropogenic warming footprint, Geophys. Res. Lett. 41 (9) (2014) 3220–3226.
[2] E.G. Paulson, REDUCING FLUORIDE IN INDUSTRIAL WASTEWATER, 1977.
[3] J. Wang, et al., Excellent fluoride removal performance by CeO2–ZrO2 nanocages in water environment, Chem. Eng. J. 231 (2013) 198–205.
[4] W. Grabow, M. Taylor, J. De Villiers, New methods for the detection of viruses: call for review of drinking water quality guidelines, Water Sci. Technol. 43 (12) (2001) 1–8.
[5] L. Chai, et al., Sulfate-doped Fe3O4/Al2O3 nanoparticles as a novel adsorbent for fluoride removal from drinking water, Water Res. 47 (12) (2013) 4040–4049.
[6] N. Rahman, M. Nasir, Development of Zr(IV)—Doped polypyrrole/zirconium (IV) iodate composite for efficient removal of fluoride from water environment, J. Water Process Eng. 19 (2017) 172–184.
[7] J. Shen, et al., Renewable energy powered membrane technology: Fluoride removal in a rural community in northern Tanzania, Sep. Purif. Technol. 149 (2015) 349–361.
[8] Y. Jia, et al., Porous 2-line ferrihydrite/bayerite composites (LFBC): fluoride removal performance and mechanism, Chem. Eng. J. 268 (2015) 325–336.
[9] S. Vasudevan, J. Lakshmi, G. Sozhan, Effects of alternating and direct current in electrocoagulation process on the removal of cadmium from water, J. Hazard. Mater. 192 (1) (2011) 26–34.
[10] S. Budyanto, Y.-L. Kuo, J. Liu, Adsorption and precipitation of fluoride on calcite nanoparticles: a spectroscopic study, Sep. Purif. Technol. 150 (2015) 325–331.
[11] K.-Y.A. Lin, Y.-T. Liu, S.-Y. Chen, Adsorption of fluoride to UiO-66-NH2 in water: stability, kinetic, isotherm and thermodynamic studies, J. Colloid Interface Sci. 461 (2016) 79–87.
[12] N. Saqib, M. Bäckström, Trace element partitioning in ashes from boilers firing pure wood or mixtures of solid waste with respect to fuel composition, chlorine content and temperature, Waste Manag. 34 (12) (2014) 2505–2519.
[13] M. Abdullah, et al., Avian feathers as a non-destructive bio-monitoring tool of trace metals signatures: a case study from severely contaminated areas, Chemosphere 119 (2015) 553–561.
[14] M. Rahaman, A. Basu, M. Islam, The removal of As (III) and As (V) from aqueous solutions by waste materials, Bioresour. Technol. 99 (8) (2008) 2815–2823.
[15] M.N. Amin, et al., Removal of arsenic in aqueous solutions by adsorption onto waste rice husk, Ind. Eng. Chem. Res. 45 (24) (2006) 8105–8110.
[16] D. Ranjan, M. Talat, S. Hasan, Biosorption of arsenic from aqueous solution using agricultural residue 'rice polish', J. Hazard. Mater. 166 (2-3) (2009) 1050–1059.
[17] T. Aman, et al., Potato peels as solid waste for the removal of heavy metal copper (II) from waste water/industrial effluent, Colloids Surf. B: Biointerfaces 63 (1) (2008) 116–121.
[18] J. Moreno-Piraján, L. Giraldo, Activated carbon obtained by pyrolysis of potato peel for the removal of heavy metal copper (II) from aqueous solutions, J. Anal. Appl. Pyrolysis 90 (1) (2011) 42–47.
[19] S. Kumar, A. Gupta, J. Yadav, Removal of fluoride by thermally activated carbon prepared from neem (Azadirachta indica) and kikar (Acacia arabica) leaves, J. Environ. Biol. 29 (2) (2008) 227.
[20] S. Al-Sulaimi, et al., Facile synthesis, structural, magnetic and enhanced Fluoride (F−1) adsorptive properties of magnesium ferrite and oryza sativa composites, Mater. Chem. Phys. 339 (2025) 130686.
[21] K. Shehzad, et al., Facile synthesis of novel calcined magnetic orange peel composites for efficient removal of arsenite through simultaneous oxidation and adsorption, J. Colloid Interface Sci. 511 (2018) 155–164.
[22] D. Li, et al., Molecular Reconstruction for the High-Performance Recycled Fluororubbers, Adv. Mater. 37 (2025) 2501622–2501633.
[23] X. Yang, et al., Ball-milled dysprosium oxide loaded biochar-montmorillonite composite for efficient removal and great recycling performance of cationic organic pollutants, Ind. Crop. Prod. 235 (2025) 121777.
[24] Y. Xu, et al., Orderly stacked 3D-nanohelices interlayer boosts performance of reverse osmosis membranes for effective water purification, Energy Environ. Sustain. 1 (1) (2025) 100003.
[25] Y. Ju-Nam, J.R. Lead, Manufactured nanoparticles: an overview of their chemistry, interactions and potential environmental implications, Sci. Total Environ. 400 (1-3) (2008) 396–414.
[26] R. Ghosh Chaudhuri, S. Paria, Core/shell nanoparticles: classes, properties, synthesis mechanisms, characterization, and applications, Chem. Rev. 112 (4) (2012) 2373–2433.
[27] K. Shehzad, et al., Facile synthesis of novel zinc ferrite nanostructures (ZFN) for enhanced adsorption of highly mobile and toxic As(III) from aqueous solutions, J. Water Process Eng. 63 (2024) 105464.
[28] L. Xie, et al., An efficient voltammetric sensing platform for trace determination of Norfloxacin based on nanoplate-like α-zirconium phosphate/carboxylated multiwalled carbon nanotube nanocomposites, Microchem. J. 206 (2024) 111451.
[29] X. Qin, H. Cui, Q. Zhou, Physisorption Behaviors of Organochlorine Pesticides on the InP3 Monolayer from Theoretical Insight, ACS Omega 8 (35) (2023) 32168–32175.
[30] D. Gaur, K. Singh, S. Upadhyaya, Experimental Study on the Removal of Toluene from Water by PTFE Hydrophobic Microporous Membrane Using Air Gap Membrane Distillation Process, Asian J. Water, Environ. Pollution 21 (3) (2024) 77–85.
[31] S.S. Staniland, Magnetosomes: bacterial biosynthesis of magnetic nanoparticles and potential biomedical applications, Online, Nanotechnologies for the Life Sciences, 2007.
[32] Q. Yuan, et al., Nano-metal oxides naturally attenuate antibiotic resistance in wastewater: killing antibiotic resistant bacteria by dissolution and decreasing antibiotic tolerance by attachment, NanoImpact 18 (2020) 100225.
[33] O. Oginni, et al., Phosphorus adsorption behaviors of MgO modified biochars derived from waste woody biomass resources, J. Environ. Chem. Eng. 8 (2) (2020) 103723.
[34] C. Wang, et al., A nanoscale ferroferric oxide coated biochar derived from mushroom waste to rapidly remove Cr (VI) and mechanism study, Bioresour. Technol. Rep. 7 (2019) 100253.
[35] F. Shahzad, et al., Enhanced peroxymonosulfate activation by ZIF-67/Bi/Ti@ NF bimetallic system for efficient antibiotic degradation, Vacuum 242 (2025) 114775–114788.
[36] G.A. Ashraf, et al., Mesoporous Carbon@ ZnCuFeS nanoparticles for photocatalytic degradation of organic pollutants via peroxymonosulfate activation, J. Organomet. Chem. 1032 (2025) 123624.
[37] M. Rashid, et al., Influence of Ni2+ ions on structural, spectral and dielectric properties of Sr–Co spinel ferrites synthesized by sol-gel auto-combustion route, Ceram. Int. 50 (13) (2024) 24679–24691.
[38] N. Kumar, et al., Synthesis of Mn 0.2 Zn 0.8 Fe 2 O 4 particles by high energy ball milling and their applications, 2009.
[39] L. Sun, et al., Effect of Zn 2+ doping on the structural, magnetic and dielectric properties of MnFe 2 O 4 prepared by the sol–gel method, J. Mater. Sci. Mater. Electron. 29 (2018) 5356–5362.
[40] H. Hejase, et al., MnZnFe nanoparticles for self-controlled magnetic hyperthermia, J. Magn. Magn. Mater. 324 (22) (2012) 3620–3628.
[41] M. Drofenik, et al., Dispersant-assisted hydrothermal synthesis of MnZn ferrites from raw oxides, J. Mater. Sci. 38 (2003) 3063–3067.
[42] W.L. Suchanek, R.E. Riman, Hydrothermal synthesis of advanced ceramic powders, in: Advances in Science and Technology, Trans Tech Publ, 2006.
[43] M. Nasir, et al., Environmentally Sustainable Hydrous Zirconium Oxide–Inulin as an Efficient Adsorbent for Ciprofloxacin Removal: Mechanistic and Thermodynamic Insights via Statistical Physics and Fractal-like Kinetic Modeling, Langmuir 41 (19) (2025) 12199–12217.
[44] N. Rahman, I. Ahmad, Insights into the statistical physics modeling and fractal like kinetic approach for the adsorption of As (III) on coordination polymer gel based on zirconium (IV) and 2-thiobarbituric acid, J. Hazard. Mater. 457 (2023) 131783.
[45] T. Tatarchuk, et al., Synthesis, morphology, crystallite size and adsorption properties of nanostructured Mg–Zn ferrites with enhanced porous structure, J. Alloys Compd. 819 (2020) 152945.
[46] N. Ahmad, S. Khan, M.M.N. Ansari, Microstructural, optical and electrical transport properties of Cd-doped SnO2 nanoparticles, Mater. Res. Express 5 (3) (2018) 035045.
[47] A.A. Ati, et al., Structural and magnetic properties of Co–Al substituted Ni ferrites synthesized by co-precipitation method, J. Mol. Struct. 1058 (2014) 136–141.
[48] D. Kurmude, et al., X-ray diffraction and cation distribution studies in zinc-substituted nickel ferrite nanoparticles, J. Supercond. Nov. Magn. 27 (2014) 547–553.
[49] M. Kurian, C. Kunjachan, Investigation of size dependency on lattice strain of nanoceria particles synthesised by wet chemical methods, Int. Nano Lett. 4 (2014) 73–80.
[50] T. Vigneswari, P. Raji, Structural, magnetic and optical properties of Al-substituted nickel ferrite nanoparticles, Int. J. Mater. Res. 109 (5) (2018) 413–421.
[51] M.Z. Khan, et al., Comprehensive study on structural, electrical, magnetic and photocatalytic degradation properties of Al3+ ions substituted nickel ferrites nanoparticles, J. Alloys Compd. 848 (2020) 155795.
[52] T. Vigneswari, P. Raji, P. Thiruramanathan, Magnetic Targeting Carrier Applications of Bismuth-Doped Nickel Ferrites Nanoparticles by Co-precipitation Method, Trans. Indian Inst. Metals 74 (9) (2021) 2255–2265.
[53] Z. Karimi, et al., Magnetic and structural properties of nano sized Dy-doped cobalt ferrite synthesized by co-precipitation, J. Magn. Magn. Mater. 361 (2014) 150–156.
[54] E. Suharyadi, et al., Magnetic properties and microstructures of polyethylene glycol (PEG)-coated cobalt ferrite (CoFe2O4) nanoparticles synthesized by coprecipitation method, Adv. Mater. Res. 896 (2014) 126–133.

[55] K. Shehzad, M.A.S. Al-Sulaimi, M. Alam, X. Chen, W. Xu, J. Liu, Facile synthesis of novel hexagonal strontium ferrites for promising adsorption of cadmium from aqueous solutions, Mater. Chem. Phys. 318 (2024) 129222.
[56] A. Ahmed, et al., Enhanced room temperature ferromagnetism in Ni doped SnO2 nanoparticles: a comprehensive study, J. Appl. Phys. 122 (8) (2017).
[57] M. Ahmad, et al., Influence of La-Substitution and SiO2 Additives on Structure, Magnetic and High Frequency Dielectric Properties of Co2W Hexagonal Ferrites Synthesized by Sol–Gel Auto-Combustion Method, J. Inorg. Organomet. Polym. Mater. (2025) 1–15.
[58] B. Rasool, et al., Insight into the structural, magnetic and fluoride (F− 1) adsorption properties of copper–manganese ferrite (Cu0· 5Mn0· 5Fe2O4) and Azadirachta Indica composites synthesized through hydrothermal method, Mater. Chem. Phys. 334 (2025) 130415.
[59] A.L. Valdivieso, et al., Temperature effect on the zeta potential and fluoride adsorption at the α-Al2O3/aqueous solution interface, J. Colloid Interface Sci. 298 (1) (2006) 1–5.
[60] M.F. Horst, V. Lassalle, M.L. Ferreira, Nanosized magnetite in low cost materials for remediation of water polluted with toxic metals, azo-and antraquinonic dyes, Front. Environ. Sci. Eng. 9 (2015) 746–769.
[61] H. Dąbkowska-Naskręt, Natural and synthetic iron oxides as adsorbents of trace elements in soils, Environ. Protect. Nat. Resources 41 (2009) 631–639.
[62] B.-S. Zhu, et al., Controlled synthesis of natroalunite microtubes and spheres with excellent fluoride removal performance, Chem. Eng. J. 271 (2015) 240–251.
[63] S. Agrawal, N. Singh, Removal of toxic hexavalent chromium from aqueous solution by nickel ferrite-polyaniline nanocomposite, Desalin. Water Treat. 57 (38) (2016) 17757–17766.
[64] M.M.S. Saif, N.S. Kumar, M. Prasad, Binding of cadmium to Strychnos potatorum seed proteins in aqueous solution: adsorption kinetics and relevance to water purification, Colloids Surf. B: Biointerfaces 94 (2012) 73–79.
[65] A. Raheem, N. Rahman, S. Khan, Monolayer Adsorption of Ciprofloxacin on Magnetic Inulin/Mg–Zn–Al Layered Double Hydroxide: Advanced Interpretation of the Adsorption Process, Langmuir 40 (25) (2024) 12939–12953.
[66] L. Liu, et al., One-step synthesis of magnetic iron–aluminum oxide/graphene oxide nanoparticles as a selective adsorbent for fluoride removal from aqueous solution, RSC Adv. 6 (13) (2016) 10783–10791.
[67] K. Shehzad, et al., Modified waste orange peels biomass residues for sustainable and promising As(V) removal: Insights into batch and column adsorption experiments and Box-behnken Design (BBD) analysis, Colloids Surf. A Physicochem. Eng. Asp. 711 (2025) 136352.
[68] G.A.A.M. Al-Hazmi, et al., Chitosan-nano CuO composite for removal of mercury (II): Box-Behnken design optimization and adsorption mechanism, Int. J. Biol. Macromol. 261 (2024) 129769.
[69] Z.A. Al-Ahmed, et al., Facile synthesis of new metal-organic framework/chitosan composite sponge for Hg(II) removal: Characterization, adsorption efficiency, and optimization using Box-Behnken design, Int. J. Biol. Macromol. 259 (2024) 129282.
[70] R. Ghubayra, et al., Synthesis and characterization of a novel TiO_2@chitosan/alginate nanocomposite sponge for highly efficient removal of As(V) ions from aqueous solutions: Adsorption isotherm, kinetics, experiment and adsorption mechanism optimization using Box-Behnken design, Int. J. Biol. Macromol. 275 (2024) 133513.
[71] X. Fu, Z. Niu, C. Peng, H. Han, W. Sun, T. Yue, Quantitative synergistic adsorption affinity of Ca(II) and sodium oleate to predict the surface reactivity of hematite and quartz, Separation and Purification Technology 360 (2025) 131196.
[72] Z. Zhang, B. Deng, Z. Cao, S. Zhang, J. Zhang, J. Zhang, S. Xia, Deep learning-based transmembrane pulsed electro-chemisorption for improved energy efficacy of recovering ammonia from wastewater, Energy & Environmental Sustainability 1 (3) (2025) 100029.
[73] F. Yan, H. Chen, T. Chi, J. Lu, X. Shen, F. Xie, Z. Zhang, Highly efficient and regenerable amine-impregnated adsorbents: Mechanistic insights into glycerol modification for enhanced direct air capture, Chemical Engineering Journal 520 (2025) 166450.
[74] H. Ma, P. Fu, J. Zhao, X. Lin, W. Wu, Z. Yu, C. Xia, Q. Wang, M. Gao, J. Zhou, Pretreatment of Wheat Straw Lignocelluloses by Deep Eutectic Solvent for Lignin Extraction, Molecules 27 (22) (2022) 7955.
[75] P. Guo, R. Xue, Q. Zou, X. Ma, C. Su, Z. Zeng, L. Li, Enhanced Ultramicropore of Biomass-Derived Porous Carbon for Efficient and Low-Energy CO2 Capture: Integration of Adsorption and Solar Desorption, ENERGY & ENVIRONMENTAL MATERIALS 70140 (2025).
[76] R. Liu, W. Ji, W. Wang, Y. Li, L. Yin, Y. Song, G. He, Innovative amorphous calcium carbonate for superior anionic dye adsorption towards near-zero discharge, Separation and Purification Technology 361 (2025) 131349.

Mukhtar Ahmad is working as a Tenured Associate Professor in the Department of Physics, COMSATS University Islamabad, Lahore Campus, Pakistan. He received his Ph.D. in Physics from Bahauddin Zakariya University, Multan, Pakistan. Prior to completing his degree, he carried out his research work at University of Technology Vienna Austria under the supervision of Prof. Dr. Roland Grossinger and conducted postdoctoral research at Institute of Intelligent Machines, Hefei Institutes of Physical Sciences, Chinese Academy of Sciences. His research focuses on inorganic chemistry, including the design and synthesis of magnetic oxides and their nanocomposites with biowastes, graphene oxide etc. for adsorbing the different pollutants from the water body, design of water treatment plants etc.